Heterogeneous crystallization in colloids and complex plasmas: the role of binary mobilities

Heterogeneous crystallization in colloids and complex plasmas: the role of binary mobilities

H Löwen[1], E Allahyarov[1], A Ivlev[2] and G E Morfill[2]

[1] Institut für Theoretische Physik II, Heinrich-Heine-Universität Düsseldorf, 40225 Düsseldorf, Germany
[2] Max-Planck-Institut für Extraterrestrische Physik, 85741 Garching, Germany

E-mail: hlowen@thphy.uni-duesseldorf.de

Abstract
Both charged colloidal suspensions and complex (dusty) plasmas represent classical many-body strongly coupled Coulomb systems. Here we discuss their basic properties and focus on their heterogeneous crystallization from an undercooled melt. In particular, a model with different mobilities is proposed which is realizable in binary mixtures of charged particles. Within this binary-mobility model, the crystallization behaviour near a structured wall is explored by Brownian dynamics computer simulations. As a result, the propagation velocity of the crystal–fluid interface is a nonmonotonic function of the mobility ratio (if expressed in terms of an averaged mobility).

(Some figures may appear in colour only in the online journal)

1. Introduction: colloids and complex plasmas

There is strong scientific activity in the field of colloidal dispersions [1–4] and in that of complex plasmas [5, 6]. Both systems allow for particle-resolved studies and provide us with excellent classical strongly coupled many-body systems to study phase transitions in equilibrium and nonequilibrium. Strong coupling here refers to the effective interaction between the big particles, i.e. the colloid or dust particles. Therefore, quite naturally, there is an interdisciplinary link between charged colloidal dispersions and complex plasmas. Colloids comprise mesoscopic particles which can be highly charged and are embedded in a liquid solvent. This makes them similar and, at the same time, different to complex plasmas: the latter are also highly charged but are embedded in a plasma, see figure 1. Static equilibrium properties only depend on the interaction forces, which are mainly screened Coulomb forces in both systems [7–13]. Within traditional linearized screening theory, the effective interaction between two charged particles (with charges Z_1 and Z_2 and radii a_1 and a_2) are given by a Yukawa pair potential [14–16]

$$V_{12}(r) = \frac{Z_1 \exp(\kappa a_1)}{1 + \kappa a_1} \frac{Z_2 \exp(\kappa a_2)}{1 + \kappa a_2} \frac{\exp(-\kappa r)}{\epsilon r} \quad (1)$$

for a given central separation[3] r. Here κ is the inverse Debye screening length[4] and ϵ is the relative dielectric constant of the solvent ($\epsilon = 1$ for the dusty plasmas). The similarity in the effective interactions results in similar behaviour for static behaviour, e.g. for the equilibrium freezing transition. The (short time) particle dynamics, however, is completely different. It is strongly overdamped (Brownian) for the colloidal particles, and ballistic (virtually undamped) for dusty plasmas.

The common advantage of colloids and complex plasmas is that the individual particle trajectories can be tracked by recording the coordinates of all particles simultaneously in real-time. This allows particle-resolved studies and gives direct insight into the nature of phase transitions and instabilities on the fundamental particle scale. Nevertheless, due to the different embedding background, there are important complementarities between colloidal

---

[3] The Yukawa interaction is justified also for small screening lengths. In this case, only the interactions stemming from nearest neighbours is relevant. Then the Yukawa interaction can also be understood as an efficient fit for the effective forces at the distance range of the first neighbour shell (with Z_i and κ playing the role of flexible fitting parameters).

[4] Strong coupling is formally defined by the condition $\Gamma = Z_1^2/k_B T a_1 \epsilon \gg 1$.
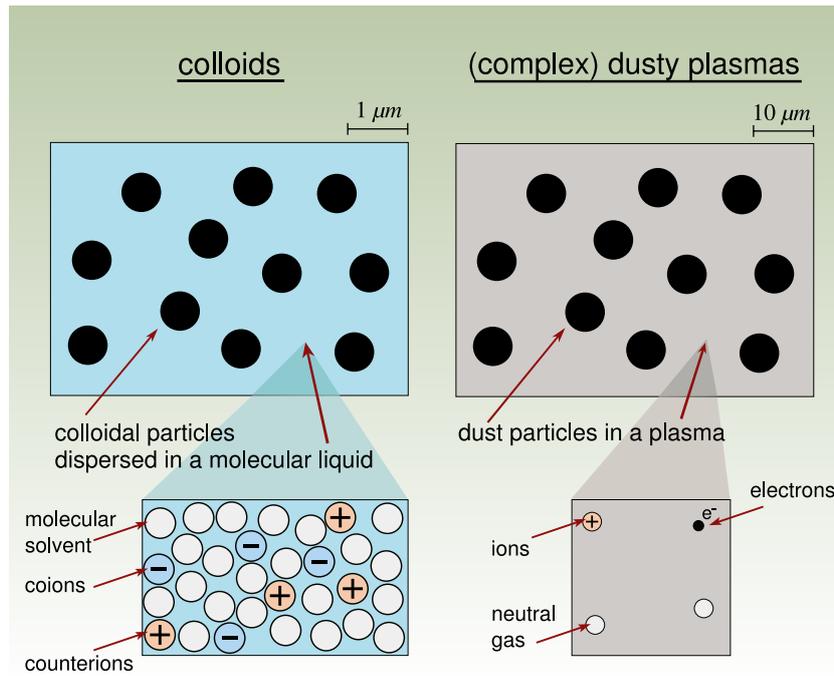
Figure 1. Schematic view of colloidal dispersions and complex plasmas: colloidal particles (black spheres in the left picture) are embedded in a molecular liquid containing also microions (counter- and co-ions) while dust particles (black spheres in the right picture) are embedded in a dilute weakly ionized gas.

dispersion and complex plasmas. Colloidal particles couple almost instantaneously to a multitude of molecules which thermalizes them efficiently. Therefore, colloidal suspensions can easily be equilibrated and are pivotal model systems if precise equilibration is needed (e.g. for the details of the two-dimensional melting process [17]). Complex plasmas, on the other hand, are typically in some quasi-equilibrium. Since the dust particles are of the order of several microns, gravity needs to be balanced by counteracting fields and therefore levitation is a harder problem for complex plasmas than for colloids, which are typically smaller and can be levitated by density-matching the solvent. This explains why a microgravity environment is essential for some complex plasma experiments.

The advantage of complex plasmas lies in their dynamics, they move almost ballistically (at timescales corresponding to, e.g. the Einstein frequency) and therefore represent big 'molecules' in the sense that they are governed by the Newtonian equation of motion. Therefore, the molecular dynamics is projected upwards to much larger length scales and correspondingly to longer timescales. This enables a dynamical resolution of ordering and flow phenomena on the particle scale. Colloids, on the other hand, are governed by completely overdamped Brownian motion. A typical example of particle trajectories is shown in figure 2. Figure 2(a) illustrates the undamped motion (close to the virtually undamped dusty plasma case), while in figure 2(b) the stochastic overdamped motion (colloids) is depicted. One can clearly see that the nature of the two trajectories is completely different.

Efficient thermalization of colloids comes at a price: moving a particle in the liquid implies a flow field of the solvent which mediates hydrodynamic interactions between neighbouring colloids. For many situations far from equilibrium, the hydrodynamic interactions cannot be neglected [1, 18, 19]. Since the interactions are long-ranged and also yield lubrication for almost touching particles, their thorough treatment is a formidable task.

Nonetheless, for some dynamical nonequilibrium properties, hydrodynamic interactions are not relevant. Then there is a strong analogy between colloids and dusty plasma for strong external drives. This explains why in both systems laning has been found [20–22] and its characterization is similar. Moreover, fluid–fluid phase separation kinetics can be resolved both in binary mixtures of dusty plasmas [23, 24] and in colloid–polymer mixtures [25, 26] revealing similar dynamical growth scenarios.

Finally, colloids and complex plasmas are both excellent model systems for crystallization and melting [27]. Real-space-imaging techniques and computer simulations yield a particle-resolved picture of freezing and melting processes, e.g. near grain boundaries [28, 29], at surfaces [30, 31] and in between external walls [32, 33].

Here we describe some results on crystallization which is initiated at a templated wall. The wall consists of fixed particles which act as an efficient nucleation seed. First of all, to highlight the link between complex plasmas and colloids, it is instructive to compare heterogeneous crystallization in a one-component Yukawa system for undamped molecular dynamics and overdamped Brownian dynamics. Second, more extensively, we study the role of the mobility ratio on crystallization in a binary system of hard spheres.

Regarding the one-component Yukawa system, all structural parameters and initial conditions were precisely
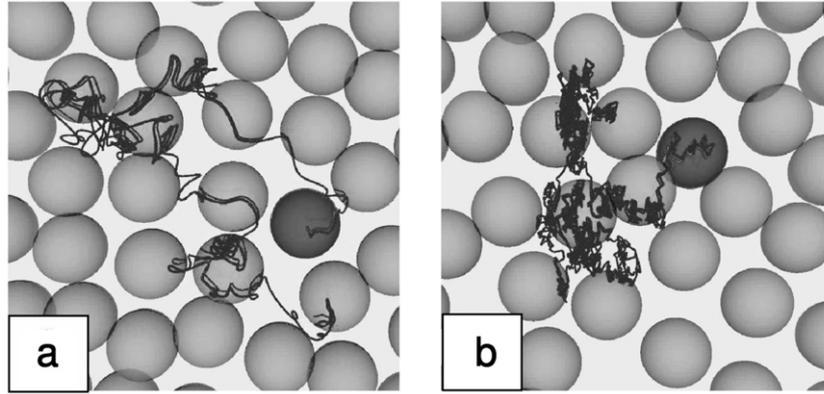
Figure 2. Typical trajectories of a tagged (black) particle for (a) Newtonian dynamics, (b) Brownian dynamics. The interaction and starting configuration (as given by the neighbouring grey spheres) are the same.

chosen to be the same such that the only difference lies in the dynamics. A wall which initializes the heterogeneous crystallization consists of particles fixed on a triangular lattice with a spacing $1.133a$ and is brought into contact with a fluid of particles with a number density $\rho_0 = 1/a^3$. Then crystalline layers grow into the fluid. The growth process can be characterized by the laterally integrated density profile $\rho(z)$ with z denoting the distance perpendicular to the wall. Peaks in $\rho(z)$ indicate a solid. In the undamped case of molecular dynamics (MD) the particle mass m induces the natural timescale ω_p^{-1} where the plasma frequency ω_p is defined via $\omega_p^2 = 4\pi\rho_0 Z^2/m$. For the overdamped Brownian dynamics (BD) the friction coefficient (or equivalently the short-time diffusion constant D_0) sets the Brownian timescale as $\tau_B = a^2/D_0$. For MD, one can further define a time-dependent laterally averaged temperature field $T(z)$ via the local kinetic energy of the particles. In equilibrium, $T(z)$ coincides with the prescribed bulk temperature T. For BD, there is instantaneous thermalization leading to $T(z) = T$ at any time. As an important physical difference between MD and BD, latent heat which is produced during the crystallization process is diffusing away for MD but immediately taken away on the Brownian timescale for BD. Due to the local heating at the interface [34] we expect that crystallization in BD is faster than for MD if considered on appropriate timescales τ_B and ω_p^{-1} respectively.

Figure 3 shows the profiles $\rho(z)$ and $T(z)$ at two different times t_1 and t_2 after starting the simulation both for MD and BD. The ratio t_1/t_2 is fixed to 5. All other system parameters are given in the caption. There are two basic messages to learn from figure 3: first, the temperature is generated at the interface and is diffusing away from the wall since the wall is modelled to be elastic. Second, by comparing the distance the crystal–fluid front has grown during the time interval $t_2 - t_1$, one can indeed conclude that the growth in BD is faster than that in MD if the time is appropriately scaled with τ_B and ω_p^{-1} respectively. In fact, for MD the crystal–fluid interface has grown for about seven layers while this shift is 11 layers for BD. This can be contributed to the local temperature increase at the interface due to latent heat production. It is only in

the limit when thermal diffusion is much faster than crystal growth that this kinetic hindering can be neglected.

Subsequently, we consider heterogeneous crystallization of a binary-mobility system of hard spheres near a wall. In our binary model we assume the same interaction diameter, but different short-time mobilities for the two species. We show that this model can be realized in binary mixtures of charged particles provided these are mapped on systems with an effective interaction diameter. As a function of the mobility ratio, this mobility-binary system exhibits a maximal crystal–fluid interfacial velocity if the latter is measured in terms of an appropriate timescale associated with the averaged mobility. The occurrence of an optimal front velocity can be exploited for practical applications and may provide some insight into the microscopic freezing kinetics of fluids in porous media modelled as random matrices with an extreme mobility asymmetry.

2. Heterogeneous crystallization near a wall for a binary-mobility system

Particle-resolved experiments on both colloids [4, 35] and complex plasmas [36] can be used to observe the details of heterogeneous crystallization kinetics induced by external inhomogeneities. The crystallization effect can be significantly modified in the presence of other external fields like gravity or external electric fields [36, 37]. Most of the features can by now be quantitatively encaptured by BD computer simulations of simple models [38, 39] (like a hard sphere model with an effective interaction diameter σ) which typically neglect hydrodynamic interactions. Under gravity, more effects were predicted by simulations, like a huge interfacial broadening [38] and a doubled heterogeneous crystallization in mass-binary mixtures [39]. These effects can in principle be verified in future real-space experiments with colloidal mixtures or dusty plasmas.

In the following we consider heterogeneous crystallization in a binary system with different short-time mobilities while keeping the interaction diameter σ the same. It is important to note that the static equilibrium quantities (like phase transition boundaries and structural correlations) are
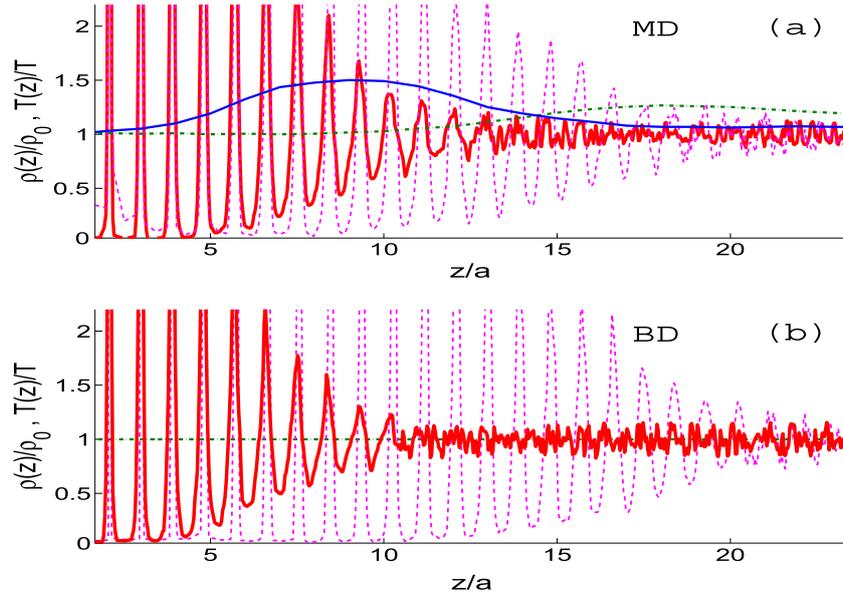
Figure 3. Simulation results for the laterally averaged particle density $\rho(z)/\rho_0$ and the temperature profile $T(z)/T$ for a one-component Yukawa system at two different times t_1 and t_2. Here, $\rho_0 = N/V$ is the average particle number density. The simulation box contains $N = 80\,000$ particles in a volume $V = L_x L_y L_z$. The laterally averaged density is defined as $\rho(z) = N(z)/(L_x L_y \Delta z)$, where $N(z)$ is the averaged number of particles inside a strip of width Δz. The simulation box has dimensions $L_x = 36a$, $L_y = 38a$, $L_x = 58a$. The bulk temperature is chosen to be $T = 2.3 \times 10^{-4} \frac{Z^2 \kappa}{k_B \epsilon}$, where $Z/e = 100$, $\epsilon = 80$ and $\kappa a = 4$. (a) Molecular dynamics (MD) simulation results. The full line (red in online version)—$\rho(z)$ at time $t_1 = 36\,000 \omega_p^{-1}$, dashed line (pink online)—$\rho(z)$ at time $t_2 = 5t_1$, thin full line (blue online)—$T(z)/T$ for $t_1 = 36\,000 \omega_p^{-1}$, dot-dashed line (green online)—$T(z)/T$ for $t_2 = 5t_1$. (b) Brownian dynamics (BD) simulation results: full line (red online)—$\rho(z)$ at time $t_1 = 3\tau_B$, dashed line (pink online)—$\rho(z)$ at time $t_2 = 5t_1$, horizontal dot-dashed line (green online)—the trivial temperature profile $T(z)/T = 1$.

identical to the one-component hard sphere system while the dynamical correlations and the nonequilibrium behaviour is different. For nonequilibrium dynamics, our model allows a link to transport processes in porous media in its limit of very high asymmetry. In this limit, one species is almost frozen-in, constituting a fixed matrix of spheres which is felt as an external obstacle (porous matrix) by the other mobile spheres [40].

2.1. Model for a binary-mobility system

Our model is an equimolar binary mixture of hard spheres with the same interaction diameter but different hydrodynamic (or physical) diameters, see the sketch in figure 4. Indeed such a mobility-binary system can in principle be realized by a charge-bidisperse mixture of colloidal particles, see e.g. [41–45], or dust particles in the plasma [21]. We describe the basic effects of the repulsions by mapping them onto an effective hard sphere system [46]. From equation (1), one sees directly that charged particle with a different charge and hydrodynamic radius can possess nevertheless the same interaction diameter provided their effective charge

$$Z_{\text{eff}}^i = Z_i \exp(\kappa a_i)/(1 + \kappa a_i)$$

is the same for $i = 1, 2$. This implies that high-charge particles with a small hydrodynamic radius can have the same effective charge as low-charge particles with a larger hydrodynamic radius. Therefore charged particles with
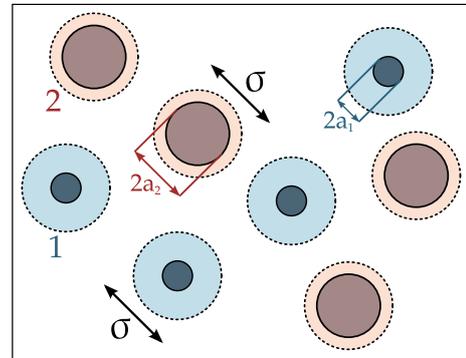

Figure 4. Sketch of the mobility-binary system. Two particle species 1 and 2 with the same interaction diameter σ but with different hydrodynamic radii a_1 and a_2 are shown. .

identical pair interactions (and therefore the same effective interaction parameter) can be vastly different in terms of their hydrodynamic radii. Of course, the effective interaction diameter should always be larger than the hydrodynamic ones, i.e. the two conditions $\sigma > 2a_1$ and $\sigma > 2a_2$ should hold, see again figure 4.

The mobility can be characterized by a short-time diffusion constant which is given in the colloidal case as $D_i = k_B T/6\pi \eta_s a_i$ for $i = 1, 2$, where $k_B T$ denotes the thermal energy and η_s the viscosity of the solvent. The mobility asymmetry as characterized by the ratio

$$\gamma = D_1/D_2 = a_2/a_1 \qquad (2)$$

can therefore be varied at fixed σ, showing that our model is realizable.

Strictly speaking, hydrodynamic interactions can only be neglected if the physical core size (i.e. the hydrodynamic diameter) is much smaller than the effective interaction diameter σ. In fact, this is realized for weakly screened charged suspensions if the Coulomb coupling is large. On the other hand, it has been shown in previous work [35] that even for hard spheres where the hydrodynamic and the interactions diameter are comparable, most of the hydrodynamic interaction can be incorporated into an effective short-time diffusion constant D_0.

Our model interpolates between two well-known models gained for the symmetric case $\gamma = 1$ and for the extreme asymmetry limit $\gamma \to \infty$. For $\gamma = 1$, we are dealing with a simple (one-component) hard sphere system. Its heterogeneous crystallization behaviour has been explored previously [35] and can serve as a reference case. The opposite limit $\gamma \to \infty$ describes mobile hard spheres in a matrix of fixed hard spheres. The thermodynamics and structure of this model have been intensely studied by theory [47–49]. Moreover, its dynamics has been explored by computer simulations [50, 51]. However, we are not aware of any crystallization study in this limit.

2.2. Computer simulation technique

We study the binary-mobility system by using BD simulations where hydrodynamic interactions are neglected [35, 38]. In detail, an equimolar mixed disordered starting configuration is used and a wall covered with hard spheres on a triangular lattice of lattice constant[5] $a = 1.133\sigma$ (corresponding to a line spacing of 0.921σ) is at the bottom of the sample at $z = 0$ (where z denotes the direction perpendicular to the wall). This will help in nucleating a crystalline sheet at the wall at time $t = 0$, which subsequently grows into the bulk.

A rectangular simulation box with dimensions L_x, L_y and L_z containing $N/2$ fast particles with mobility D_1 and $N/2$ slow particles with mobility D_2 is considered. In total, $N = 80\,000$ particles were simulated. The mobility asymmetry $\gamma = D_1/D_2$ is varied in the range between 1 and 20. The initial homogeneously mixed fluid configuration has a volume fraction

$$\eta = \frac{\pi \sigma^3}{6} \frac{N}{L_x L_y L_z} \tag{3}$$

which is another system parameter defining the 'undercooling' (or 'overpacking') of the fluid initial state relative to the stable solid.

In order to identify trends as a function of the mobility ratio γ, we define an averaged timescale $\tau_3 = \sigma^2/D_3$ where D_3 is the arithmetic mean of the two diffusion constants, $D_3 = (D_1 + D_2)/2$. This averaged time can also be rewritten as

$$\tau_3 = \tau_1 \frac{2\gamma}{1+\gamma} \tag{4}$$

---

[5] A more systematic exploration of the dependence of crystallization on the substrate lattice constant was recently performed in [52].

with $\tau_1 = \sigma^2/D_1$. We appropriately rescale the simulation time as $t^* = t/\tau_3$ and compare the behaviour of different systems at a given t^* for different undercoolings η and asymmetries γ.

Crystalline particles are identified with a common q_6-criterion [35, 38]. All other particles are called liquid-like. In order to identify the crystal–fluid interface, we define a laterally averaged profile $\phi(z, t)$ of the volume fraction. Furthermore, laterally averaged number densities $n_c(z, t)$ and $n_\ell(z, t)$ for the crystalline and liquid-like particles are defined.

3. Results

Simulation results for the laterally averaged volume fraction $\phi(z, t)$ and the laterally averaged number densities $n_c(z, t)$ and $n_\ell(z, t)$ are shown in figure 5 after a time $t = 10\tau_3$. Three different values of γ are explored at fixed packing fraction of $\eta = 0.52$. The $\phi(z, t)$ exhibits three parts: a crystalline part touching the wall at $z = 0$ which has huge density peaks (maxima are not shown), an interfacial region comprising about eight crystalline layers, and a fluid part for large distances z. The data reveal a width of the q_6-interface of about 5σ which is more or less independent of γ.

The position $z_0(t)$ of the crystal–fluid front can directly be located by the intersection point of the crystalline and liquid-like particle profiles, see the full and broken lines in figure 5. Interestingly, the front position depends nonmonotonically on the mobility ratio γ. This trend holds also for longer times as documented in figure 6, where the corresponding laterally averaged volume fractions are shown for $t = 100\tau_3$. It is important to note that there is no segregation between fast and slow particles. Both partial volume fractions are (to a good approximation) half of the total volume fraction $\phi(z, t)$.

In order to get more intuitive information about the interfacial structure we consider typical simulation snapshots of the crystalline particles. These allow us to have a direct instantaneous view on the fluid–solid interface. Simulation snapshots after a time $t = 50\tau_3$ are shown in figure 7 for $\eta = 0.52$ and three different values of γ. As expected, the nonmonotonic behaviour is clearly visible here as well but the snapshots also reveal a considerable roughness of the crystal–fluid interface.

We have finally plotted the propagated distance of the crystal–fluid interface $z_0(t)$ after a time of $t = 50\tau_3$ for various mobility ratios γ and four different bulk packing fractions η in figure 8. We see that z_0 attains a maximum at a small dynamical asymmetry γ_{max} and then decreases substantially at large γ. The inset of figure 8 clearly shows that γ_{max} increases with bulk packing fraction η, but the increase is small. It is important to note that the timescale must be chosen to be some average of the two individual timescales to see this maximum. If the growth velocity is expressed in terms of the individual timescales $\tau_1 = \sigma^2/D_1$ or $\tau_2 = \sigma^2/D_2$, there is no maximum. However, if the geometric mean of τ_1 and τ_2 is taken as a timescale, the maximum persists. Clearly, the maximum would also have occurred if another time (e.g. $t = 20\tau_3$ instead of $t = 50\tau_3$) had been taken. We have further made sure that
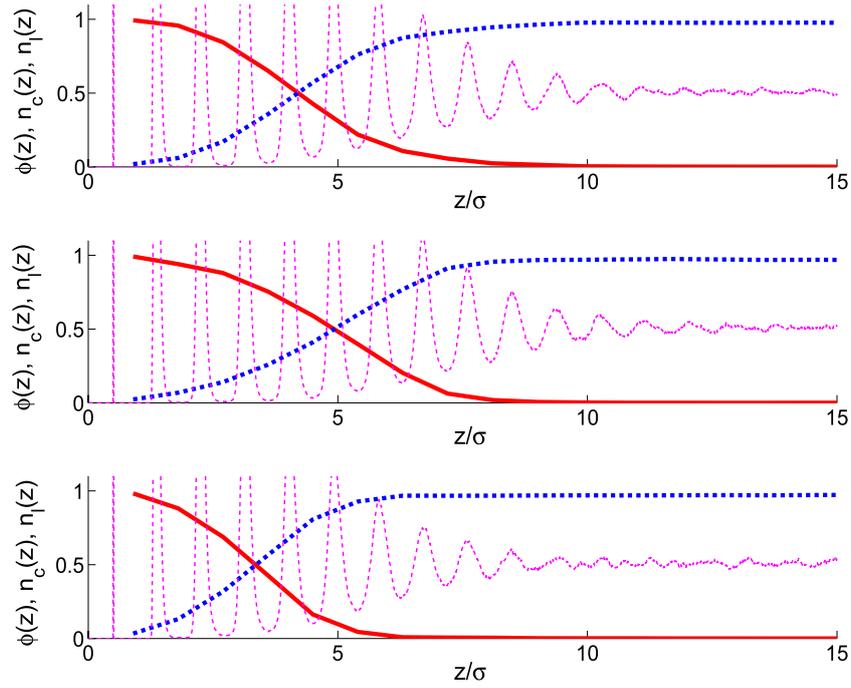
Figure 5. Simulation results for laterally averaged packing fractions $\phi(z)$ for $\eta = 0.52$ at $t = 10\tau_3$. From top to bottom the parameter $\gamma = D_1/D_2$ is changed as 1.1, 1.25, and 5. Dashed line (pink in online version)—$\phi(z)$, thick full line (red online)—interfacial profile $n_c(z)$ for the 'crystalline' particles, thick dashed line (blue online)—interfacial profile $n_l(z)$ for the 'liquid-like' particles.
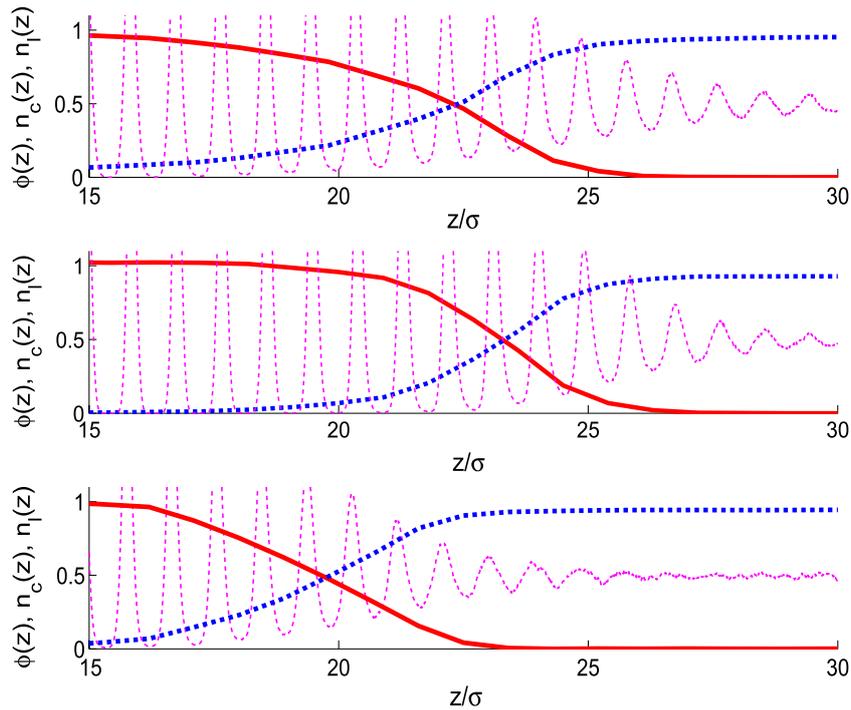

Figure 6. Same as figure 5, but now for $t = 100\tau_3$.

the nonmonotonicity persists if a q_6 threshold value different from 0.5 is used to define the interface position.

In order to further check the stability of the nonmonotonicity, we have plotted the front velocity v defined as

$$v = \frac{z_0/\sigma}{\tau_3/\tau_1} = \frac{z_0/\sigma}{2\gamma/(1+\gamma)} \qquad (5)$$

after a time $t = 50\tau_3$ for various mobility ratios γ and four different bulk packing fractions η. One should bear in mind that this front velocity is scaled with respect to τ_3, i.e. it measures the distance the interface position travels within the time τ_3. Figure 9 shows that at lower values of η the front velocity v attains a maximum at a small dynamical asymmetry
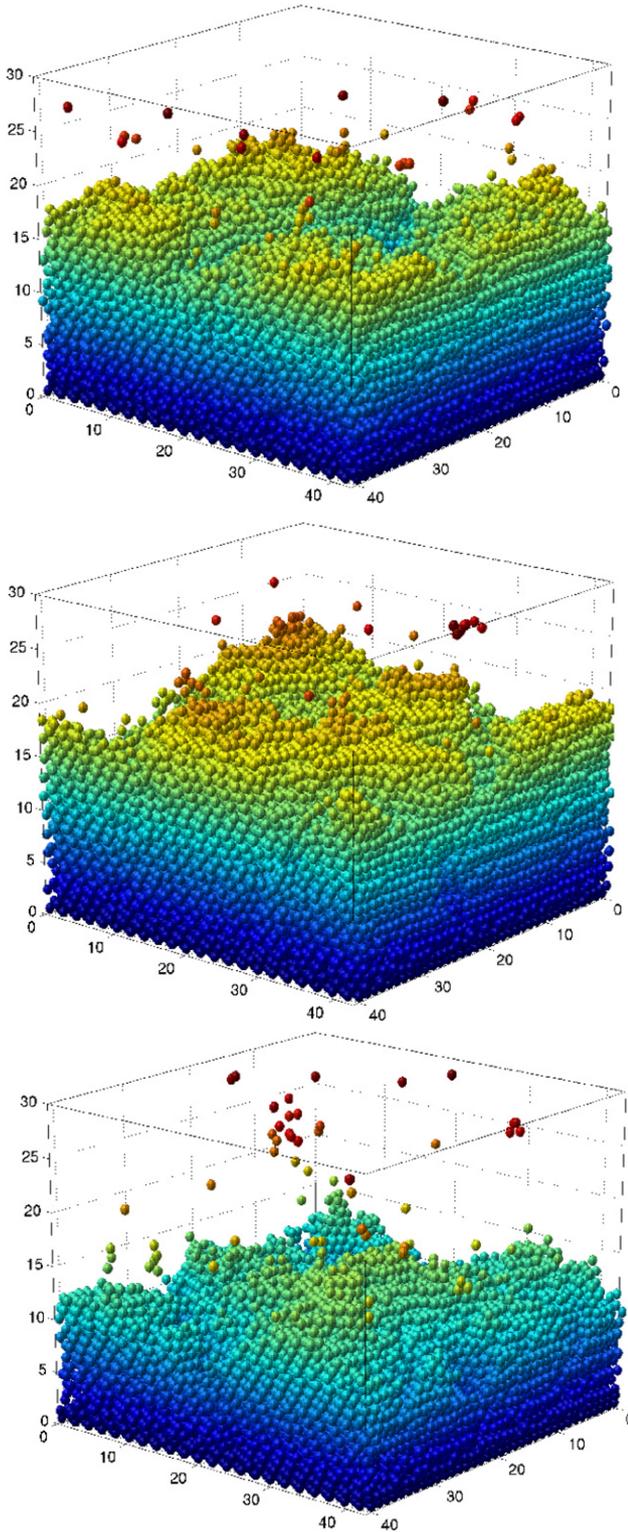
Figure 7. Simulation snapshots of crystalline particles after a time $t = 50\tau_3$ for $\eta = 0.52$. From top to bottom: $\gamma = 1.1$, 1.25 and 5.

Figure 8. Simulation results for the crystal–liquid front position z_0 for different bulk packing fractions η at $t = 50\tau_3$ as a function of the mobility ratio $\gamma = D_1/D_2$. The inset shows the dependence of the value γ_{max} at which z_0 is maximal on the bulk packing fraction η. The error bars are no larger than the symbol size used.

Figure 9. Simulation results for the crystal–fluid front velocity v for different bulk packing fractions at $t = 50\tau_3$ as a function of the mobility ratio $\gamma = D_1/D_2$. The parameter γ_{max}, which corresponds to the values of γ at which the front velocity reaches a maximum value is shown in the inset. The error bars of calculated velocities do not exceed the size of the symbols used.

γ_{max} and then decreases substantially at large γ. The actual values for γ_{max} (see insets of figures 8 and 9) are similar but not exactly the same.

Our intuitive explanation for the optimal growth velocity (corresponding to the maximum in the propagated distance) at sma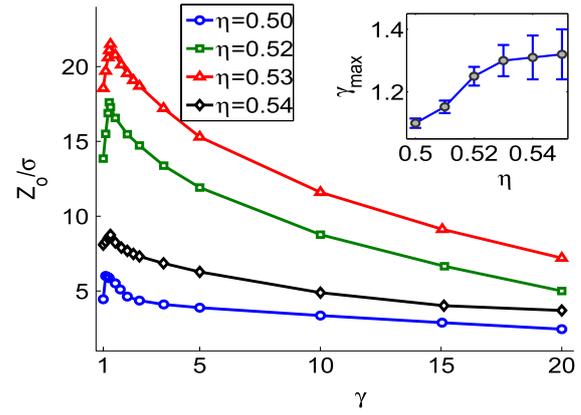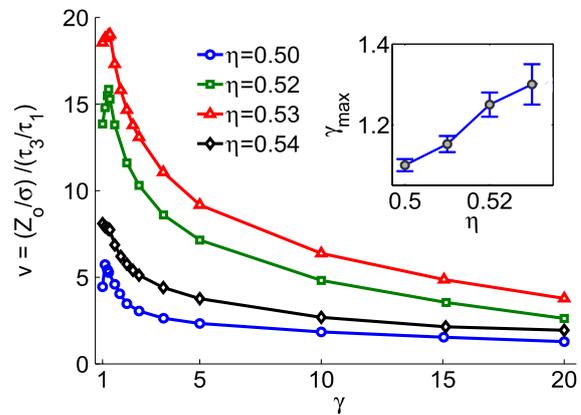ll undercooling $\eta < 0.54$ is as follows: let us consider slightly asymmetric systems where γ is a bit larger than 1. Starting from an initial disordered configuration, the undercooling forces both particle species to find positions which are crystal-like. The faster particles will find such a position on a timescale of order τ_1 more quickly than the slower particles. Once the faster particles are at a crystal-like position, this will accelerate the motion of the smaller particles towards their optimal crystal-like positions. Hence they will get there a bit faster than supposed for an uncorrelated picture. Altogether, when considered on the species-averaged timescale τ_3, a binary mobility will accelerate the dynamics of crystallization, i.e. v will increase with γ. On the other hand, in the extreme limit of very large γ, the slow particles will act as immobile obstacles for the crystallization of the fast particles ('limit of a porous matrix'). Hence fast particles have to crystallize in a complex surrounding, which slows down the crystallization considerably. Consequently, there must be an optimal ratio of mobilities where the growth velocity is maximal.

At large undercooling ($\eta = 0.54$), the reduction in the kinetic prefactor (or in the long-time self-diffusion coefficient) leads to the fact that z_0 is getting smaller although the thermodynamic drive is larger, see again figure 8. Neighbouring particles are forced to move as clusters at these high densities such that the picture of subsequent individual motion of fast and slow particles breaks down. This gives an insight into why there is no nonmonotonicity for $\eta > 0.53$.

The occurrence of an optimal mobility ratio can be exploited to steer crystal growth in mixtures. In particular, quick crystallization can be induced by using mixtures almost symmetric in their mobility.

We finally comment that, for the colloids moving in a matrix of fixed obstacles, as obtained formally in the limit of $\gamma \to \infty$ hydrodynamic interactions can be neglected if the matrix has particles with a large interaction diameter and a small core size. Such a model matrix can be realized by fixing many strongly charged colloids at matrix position by using optical tweezers.

4. Conclusions

In conclusion, charged colloidal dispersions and complex plasmas share the feature of a classical strongly coupled Coulomb system. Both systems are ideal model systems to study freezing and melting processes on the particle scale in order to unravel the processes of crystal nucleation and growth. Binary mixtures with different short-time mobilities show an important effect of the mobility asymmetry on the speed of crystal growth. For small asymmetries, crystallization becomes faster while for large asymmetries the fast particles freeze first feeling the slow particles as obstacles, which slows down the crystallization process as compared to the one-component system.

Future work should explore different interaction radii of the species. Moreover, the limit of high mobility asymmetry should be considered more in order to work out the link to fluids in disordered porous media [40].

Acknowledgments

References

[1] Pusey P N 1991 *Liquids, Freezing and the Glass Transition* ed J P Hansen, D Levesque and J Zinn-Justin (Amsterdam: North-Holland)
[2] Hansen J-P and Löwen H 2000 *Ann. Rev. Phys. Chem.* **51** 209
[3] Löwen H 2010 *Soft Matter* **6** 3133
[4] Chen D *et al* 2010 *Annual Review of Condensed Matter Physics* vol 1, ed J Langer (Palo Alto: Annual Reviews) p 301
[5] Morfill G E and Ivlev A 2009 *Rev. Mod. Phys.* **81** 1353
[6] Morfill G E, Ivlev A, Brandt P and Löwen H 2010 *CP1242 Plasmas in the Laboratory and in the Universe: Interactions, Patterns, and Turbulences* (*Centro di Cultura Scientifica*) ed G Bertin *et al* (Melville, NY: AIP) pp 67–79
[7] Löwen H and Kramposthuber G 1993 *Europhys. Lett.* **23** 673
[8] Bitzer F *et al* 1994 *Phys. Rev.* E **50** 2821
[9] Monovoukis Y and Gast A 1989 *J. Colloid Interface Sci.* **128** 533
[10] Sirota E B *et al* 1989 *Phys. Rev. Lett.* **62** 1524
[11] Löwen H and Allahyarov E 1998 *J. Phys.: Condens. Matter* **10** 4147
[12] Baumgartl J, Arauz-Lara J L and Bechinger C 2006 *Soft Matter* **2** 631
[13] Khrapak S, Ivlev A and Morfill G E 2010 *Phys. Plasmas* **17** 042107
[14] Mendez-Alcaraz J M, D'Aguanno B and Klein R 1991 *Physica* A **178** 421
[15] Krause R, D'Aguanno B, Mendez-Alcaraz J M and Klein R 1991 *J. Phys.: Condens. Matter* **3** 4459
[16] Allahyarov E and Löwen H 2009 *J. Phys.: Condens. Matter* **21** 1
[17] Zahn K, Lenke R and Maret G 1999 *Phys. Rev. Lett.* **82** 2721
[18] Nägele G 1996 *Phys. Rep.* **272** 216
[19] Dhont J 2003 *An Introduction to Dynamics of Colloids* (Amsterdam: Elsevier)
[20] Dzubiella J, Hoffmann G P and Löwen H 2002 *Phys. Rev. E* **65** 021402
[21] Sütterlin K R *et al* 2009 *Phys. Rev. Lett.* **102** 085003
[22] Vissers T *et al* 2011 *Soft Matter* **7** 2352
[23] Ivlev A, Zhdanov S, Thomas H M and Morfill G E 2009 *Europhys. Lett.* **85** 45001
[24] Wysocki A *et al* 2010 *Phys. Rev. Lett.* **105** 045001
[25] Royall C P, Aarts D G A L and Tanaka H 2007 *Nature Phys.* **3** 636
[26] Otsuka T, Royall C P and Tanaka H 2008 *Europhys. Lett.* **84** 46002
[27] Löwen H 1994 *Phys. Rep.* **237** 249
[28] Alsayed A M *et al* 2005 *Science* **309** 1207
[29] Pusey P N 2005 *Science* **19** 1198
[30] Löwen H, Beier T and Wagner H 1989 *Europhys. Lett.* **9** 791
[31] Godonoga M, Malins A, Eggers J and Royall C P 2011 *Mol. Phys.* **109** 1393
[32] Messina R and Löwen H 2003 *Phys. Rev. Lett.* **91** 146101
[33] Fontecha A *et al* 2005 *J. Phys.: Condens. Matter* **17** S2779
[34] Löwen H, Bechhoefer J and Tuckerman S 1992 *Phys. Rev. A* **45** 2399
[35] Sandomirski K, Allahyarov E, Löwen H and Egelhaaf S U 2011 *Soft Matter* **7** 8050
[36] Rubin-Zuzic M *et al* 2000 *Phys. Rev. Lett.* **85** 4064
[37] Dullens R, Aarts D G A L and Kegel W 2006 *Phys. Rev. Lett.* **97** 228301
[38] Allahyarov E and Löwen H 2011 *Europhys. Lett.* **95** 38004
[39] Löwen H and Allahyarov E 2011 *J. Chem. Phys.* **135** 134115
[40] Kurzidim J, Coslovich D and Kahl G 2009 *Phys. Rev. Lett.* **103** 138303
[41] Meller A and Stavans J 1992 *Phys. Rev. Lett.* **68** 3646
[42] Okubo T and Fujita H 1996 *Colloid Polym. Sci.* **274** 368
[43] Lorenz N J *et al* 2009 *J. Phys.: Condens. Matter* **21** 464116
[44] Lorenz N J and Palberg T 2010 *J. Chem. Phys.* **133** 104501
[45] Wette P, Schöpe H J and Palberg T 2009 *Phys. Rev.* E **80** 021407
[46] See e.g. Löwen H, Roux J N and Hansen J P 1991 *J. Phys.: Condens. Matter* **3** 997
[47] Schmidt M 2002 *Phys. Rev.* E **66** 041108
[48] Holovko M and Dong W 2009 *J. Phys. Chem. B* **113** 6360
[49] Patsahan T, Holovko M and Dong W 2011 *J. Chem. Phys.* **134** 074503
[50] Chang R, Jagannathan K and Yethiraj A 2004 *Phys. Rev. E* **69** 051101
[51] Sung B J and Yethiraj A 2007 *J. Chem. Phys.* **126** 034704
[52] Dorosz S and Schilling T 2012 *J. Chem. Phys.* **136** 044702